Multi-Component Crosslinked Hydrogel Electrolyte Toward Dendrite-Free Aqueous Zn Ion Batteries with High Temperature Adaptability

Hongyu Lu,[+] *Jisong Hu,*[+] *Litong Wang,*[+] *Jianzhu Li, Xiang Ma, Zhicheng Zhu, Heqi Li, Yingjie Zhao, Yujie Li,*[*] *Jingxin Zhao,*[*] *Bingang Xu*[*]

[*] H. Lu, J. Li, Prof. Y. Li

State Key Laboratory of Advanced Welding and Joining, Harbin Institute of Technology, Harbin 150001, P. R. China

E-mail: liyujie@hit.edu.cn

H. Lu, J. Li, X. Ma, Z Zhu, H.Li, Y. Zhao, Prof. Y. Li

School of Materials Science and Engineering, Harbin Institute of Technology (Weihai), Weihai 264209, P. R. China

J. Hu

School of Optical and Electronic Information, Huazhong University of Science and Technology, Wuhan 430074, P. R. China

L. Wang

Joint Key Laboratory of the Ministry of Education, Institute of Applied Physics and Materials Engineering, University of Macau, Avenida da Universidade, Taipa, Macau SAR 999078, P. R. China

Dr. J. Zhao, Prof. B. Xu

Nanotechnology Center, Institute of Textiles and Clothing, The Hong Kong Polytechnic University, Hung Hom, Kowloon, Hong Kong 999077, P. R. China

E-mail: jingxzhao@polyu.edu.hk, tcxubg@polyu.edu.hk

[+] These authors contributed equally to this work.

Keywords: Hydrogel electrolytes, Zn dendrites, highly reversible Zn anodes, aqueous Zn ion battery, wide-temperature range

Abstract:

Rechargeable aqueous Zn-ion batteries (ZIBs) are always regarded as a promising energy storage device owing to their higher safety and durability. However, two problems have become the main trouble for the practical application of ZIBs such as the dendrite growth of Zn metal anode in electrolyte and the freezing of water solvent at low temperature. Herein, to overcome these challenges, a new strategy of multi-component crosslinked hydrogel electrolyte is proposed to inhibit Zn dendrites and realize low temperature environmental adaptability for ZIBs. Specifically, the polyacrylamide (PAAm) chains with zincophilic group are used as hydrogel electrolyte skeleton to coordinate with Zn ions to achieve stable Zn plating/stripping. Meantime, incorporating the organic additive of Dimethyl sulfoxide (DMSO) into hydrogel electrolyte can further prevent Zn dendrite growth owing to the decomposition of solvated DMSO induced formation of the solid-electrolyte interphase（SEI). Moreover, the stronger hydrogen bonds of H_2O/DMSO binary solutions lead to vastly reduced freezing temperature. Benefitting from the superior inhibition effect of PAAm and DMSO on Zn dendrites, the coulombic efficiency (CE) of Zn/PDZ-H//Zn/PDZ-H symmetric cell of ~ 99.5 % is achieved during the Zn plating/stripping over 1,300 h, and the assembled full-cell demonstrates the large specific capacity of 265.2 mAh g^{-1} and high cyclic stability with the capacity retention of 95.27 % after 3,000 cycles. In addition, the full-cell delivers the stable operation at a wide temperature range from 60 °C to - 40 °C. This work provides an inspired strategy and novel opportunities to realize a dendrite-free and wide-temperature rechargeable aqueous Zn-ion energy storage system.

1. Introduction

Lithium-ion batteries (LIBs) have been extensively utilized in portable electronics owing to their high energy density and long-term cyclic performance.[1-3] However, serious safety issues are exposed when LIBs with organic electrolyte are used for mobile phones and electric vehicles.[4] Rechargeable aqueous ZIBs have gained widespread attention as an alternative candidate to LIBs owing to the usage of water as the electrolyte solvent, which can effectively decrease safety issues caused by flammable electrolyte.[5-9] In addition, Zn metal is often used as the anode of ZIBs owing to their inherent advantages such as high theoretical capacity of 820 mAh g^{-1} and low redox potential (- 0.76 vs SHE).[10] However, the severe dendrite growth in alkaline electrolyte can lead to the unavoidable short circuit and then capacity attenuation of ZIBs.[11-13] To resolve the aforementioned issues, many strategies for electrolyte optimization have been proposed, such as utilizing the concentrated electrolyte, introducing additives into the electrolytes and designing hydrogel electrolyte.[14-16] Unfortunately, the high-concentrated "water-in-salt" electrolyte containing salts with extremely expensive price is not beneficial to the practical application in energy storage devices.[17] While introducing the organic polymer additives into electrolytes will cause the inordinate adhesion of polymer, thus resulting in the excessive polarization of the Zn metal anode and the inferior electrical conductivity of electrode.[18] Conventional hydrogel electrolyte does restrict the dendrite growth, but the gel electrolytes without cross-linking that is demonstrated to be liquidity may suffer from deformation and damage at the harsh environment.[19]

Cross-linked hydrogel based on PAAm has been reported and served as quasi-solid electrolyte and separator in ZIBs because of its excellent mechanical property and high ionic conductivity.[20] More importantly, the carbonyl groups with negative charge in PAAm chain can block active water molecules and coordinate with Zn ions to improve their distribution, which can restrict the dendrite growth of Zn metal anode.[21] Nevertheless, the strong coulombic interaction between the Zn ions and active water molecules during Zn dissolution/deposition process boosts the decomposition of the solvated water molecules and the dendrite growth of Zn metal anode at a high overpotential. To decrease the water activity, solvent additives with higher Gutmann donor number than water should be introduced into hydrogel electrolyte owing to their strong hydrogen bond with water molecules.

As a low-cost and highly polar aprotic organic solvents, the DMSO possesses a high dielectric constant of 47.2 and donor number of 29.8.[22] Hence, DMSO embraces the unique characteristic that is a good medium to form hydrogen bond with water molecules, and thus restricts their activities. Very recently, Wang and co-workers have reported that introducing DMSO as an additive into aqueous electrolyte can inhibit the passivation of Zn surface and increase the Zn dissolution/deposition.[23]

Herein, we developed a PAAm/DMSO/$Zn(CF_3SO_3)_2$ multi-component hydrogel electrolyte (Defined as PDZ-H electrolyte) for aqueous ZIBs by adopting the PAAm as a cross-linked polymeric framework, DMSO as an organic additive and $Zn(CF_3SO_3)_2$ as Zn salts, which can be utilized to improve the reversibility of Zn metal anode at microscale. Specifically, 1) the abundant functional groups with negative charge on PAAm chains can be coordinated with Zn ions, which can restrict the cusp effect and attract more accumulation of Zn salts, and thus suppress the growth of Zn dendrites in repeated charge/discharge process. 2) The additive DMSO can further suppress the formation of Zn dendrites owing to preferential reduction of solvated DMSO to form SEI on Zn anode.[23] Therefore, the novel PDZ-H electrolyte based on PAAm and DMSO additive enables the realization of the uniform Zn deposition. Benefitting from the excellent synergistic effect of the PAAm and DMSO, the emerging PDZ-H electrolyte have demonstrated a high CE of 99.5 % during Zn plating/stripping over 1,300 h. The resulting full cells based on $Zn_3V_2O_8$ cathode and PDZ-H electrolyte achieve a large capacity of 265.2 mAh g^{-1}, high energy density of 412.3 Wh kg^{-1}, and long-term cycle performance together with splendid temperature adaptability.

2. Results and Discussions

2.1 Fabrication and Structural Characterization of the PDZ-H Electrolyte

The preparation process of PDZ-H electrolyte with good flexibility is illustrated in **Figure 1**a, and the specific experimental details are provided in experimental section. In addition, the hydrogel electrolyte containing PAAm and $Zn(CF_3SO_3)_2$ (Defined as PZ-H electrolyte) and pure PAAm hydrogel (Defined as P-H electrolyte) are also fabricated. The scanning electron microscope (SEM) image in Figure 1b shows that synthesized PDZ-H electrolyte possesses the continuous network architecture and interconnected pores, and the pore size of 2 ~ 6 μm and a high specific surface area of 359 m^2 g^{-1} are obtained (Figure S1, Supporting Information). This ensures an adequate water content of the aqueous electrolyte and provides fast Zn ion transport paths. Figure 1c exhibits that the PDZ-H electrolyte still retains an impressive flexibility without fracture even under twisting and stretching. And it can be molded into various shapes, which further demonstrate its excellent flexibility performance (Figure 1d). Moreover, the PDZ-H electrolyte does not turn into an ice-like solid state even at - 40 °C due to the existing of DMSO (Figure 1e-i). Figure 1j demonstrates the Raman spectras of the PDZ-H, PZ-H and P-H electrolyte, respectively. The vibration band located at 350, 750, 835, 1104, 1290 and 1425 cm^{-1} correspond to δ(C-C-C), polymer vibration, v(C-C) side-chain, C-C skeletal stretching, C-H bending and C-N stretching (amide III) of PAAm hydrogel electrolyte, respectively.[23, 24] In addition, the stretching mode of the sulfoxide (S=O) group of the additive DMSO is achieved at 1050 cm^{-1}.[23] The typical strain-stress curves in Figure 1k reveal that the PDZ-H electrolyte embraces a high tensile strength of 48.8 kPa and a large fracture elongation of 1,122 %. More importantly, the maximum strain of the PDZ-H electrolyte is about 2.5 times of the P-H electrolyte. As shown in Figure 1l, the ionic conductivity of PDZ-H electrolyte increases with the increase of environmental temperature, demonstrating an excellent temperature adaptability of the PDZ-H electrolyte.

2.2 Structural Characterization and Electrochemical Properties of Dendrite-Free Zn Anode

The reversibility and stability of Zn metal anode with the PDZ-H electrolyte (denoted as Zn/PDZ-H) and with Zn $(CF_3SO_3)_2$ aqueous electrolyte (denoted as Zn/Z-AE) are investigated by electrochemical measurements. **Figure 2**a shows the cyclic voltammetry (CV) curves of Zn/PDZ-H and Zn/Z-AE anodes at a scan rate of 2 mV s^{-1} between - 0.7 to - 1.2 V. It can be seen that the Zn/PDZ-H anode embraces a pair of redox peaks located at - 0.78/- 1.20 V, which corresponds to the stripping/plating process of Zn/Zn^{2+}. In addition, the high response current and low potential of the Zn/PDZ-H anode indicate their fast kinetics during Zn plating/stripping process.[25] The linear polarization curves illustrated in Figure 2b represent that the corrosion potentials of Zn/PDZ-H and Zn/Z-AE anodes are - 0.995 and - 1.012 V, respectively. It is obvious that the corrosion potential of Zn/PDZ-H anode shifts to a positive potential, which reveals that the corrosion-resistance of Zn anode increases owing to the protective effect of the PDZ-H electrolyte.[26] Moreover, the low charge transfer resistance (R_{ct}) of the Zn/PDZ-H anode demonstrates more efficient charge transfer process for faster plating kinetics, which is attribute to the high ion conductive network and rich active sites within the PDZ-H electrolyte (Figure 2c).[27] To investigate the reversibility of Zn plating/stripping, the long-term galvanostatic cycling performance of Zn/PDZ-H and Zn/Z-AE anodes are performed in symmetric cells for different current densities. Notably, the Zn/PDZ-H//Zn/PDZ-H symmetrical cell displays a stable voltage profile with a low voltage hysteresis of ~ 36 mV and a withstand lifespan over 1,350 h at a current density of 2 mA cm^{-2} with a limited capacity of 4 mAh cm^{-2}, while the Zn/Z-AE//Zn/Z-AE symmetric cell shows a immense voltage fluctuation after 140 h, which ascribes to the dynamic dendrite-induced soft short-circuit (Figure 2d). Figure S2 in the Supporting Information shows the 2th, 50th and 300th cycles of Zn/PDZ-H//Zn/PDZ-H and Zn/Z-AE//Zn/Z-AE symmetric cell in Figure 2d, demonstrating the excellent stability of the Zn/PDZ-H anode. In addition, the impressive durability of the Zn/PDZ-H anode is further confirmed by the long-term cycling measurement at a high current density of 5 mA cm^{-2} with a limited capacity of 10 mAh cm^{-2} (Figure 2e), and the curves of 2th, 30th and 200th cycles are also exhibited in Figure S3 (Supporting Information). From Figure 2e, the Zn/PDZ-H anode achieves a stable voltage hysteresis of 141 mV without evident oscillation over 800 h, while the unstable voltage response of Zn/Z-AE is observed after 50 h. Even at the current density of 10 mAh cm^{-2}, the Zn/PDZ-H anode also manifests a superior stability (Figure S4, Supporting Information). Figure 2f displays the rate performances of Zn/PDZ-H and Zn/Z-AE anodes at different current densities from 0.5 to 5 mA cm^{-2}, in which the Zn/Z-AE anode always embraces a higher voltage hysteresis than that of the Zn/PDZ-H anode, especially at a high current density. In addition, the voltage hysteresis of the Zn/PDZ-H anode is nearly unchanged when the current density is shifted back to the initial current density of 0.5 mA cm^{-2}, which demonstrates a low polarization and satisfactory stability of the Zn/PDZ-H anode. The CE is an important factor for evaluating the reversibility of Zn plating and stripping. As illustrated in Figure 2g, the Zn/Z-AE anode fails to work after 35 cycles at 2 mA cm^{-2} with a limited capacity of 4 mAh cm^{-2}. Whereas the Zn/PDZ-H anode exhibits a prominently improved CE, delivering an average CE of 99.5 % within 330 cycles. Figure 2h reveals that the voltage hysteresis of the Zn/PDZ-H anode is ~ 0.11 V, which is much lower than that of the Zn/Z-AE anode (Figure 2i), and the discharge curves of Zn/PDZ-H anode are longer than those of Zn/Z-AE anode in the time scale, indicating a less irreversible capacity loss of the Zn/PDZ-H anode.[28] The electrochemical performance of the as-fabricated Zn metal anode with PAAm/Zn(CF_3SO_3)$_2$ hydrogel electrolyte (defined as Zn/PZ-H) is also accurately assessed (Figure S5, Supporting Information), and the corresponding details are described in the Supporting Information.

The above results are mainly ascribed to the accumulation of Zn dendrites on the Zn anode. The proposed schematic illustrations of Zn plating on Zn/Z-AE and Zn/PDZ-H anodes are graphically illustrated in **Figure 3**a. To accurately verify the short-circuit induced failure mechanism of the Zn anode, the morphologies of Zn/PDZ-H and Zn/Z-AE at different cycling times are characterized by a laser confocal scanning microscope (LCSM) and SEM. Figure 3b-d show the LCSM images of the Zn/Z-AE anode at different cycling time (0 h, 50 h and 200 h). The pristine Zn/Z-AE anode possesses a smooth 2D planar structure (Figure 3b). Peaks and valleys can be clearly observed in Figure 3c,d. The surface of Zn/Z-AE anode become rougher with the increase of cycling time. However, the roughness on the surface of the Zn/PDZ-H anode just changed slightly when the cycling time increases from 50 h to 1,350 h (Figure 3e-g).

Figure 3h-j and Figure 3k-m exhibits the morphological evolution of Zn/Z-AE and Zn/PDZ-H anodes with respect to the plating time, respectively. The SEM images of Zn/PDZ-H and Zn/Z-AE anodes at the initial state both embrace smooth and flat surfaces (Figure 3h,k). Figure 3i displays the SEM image of the Zn/Z-AE anode after Zn plating of 50 h at a current density of 2 mA cm^{-2}. A large amount of vertical flakes are formed on the surface of the Zn/Z-AE anode. As shown in Figure 3j, the dense Zn vertical flakes further transformed into Zn dendrites with a size of ~ 2 μm. The dendrites cover on the surface of the Zn/Z-AE anode to form a bumpy surface at the cycling time of 200 h. The rapid growth of Zn dendrites means that an extremely uneven Zn deposition occurs on the surface of the Zn/Z-AE anode during Zn plating process, and corresponding serious hydrogen evolution reaction (HER) evolution lead to the unstable interface behaviors.[29] Whereas, the Zn/PDZ-H anode exhibits its surface to be smooth and flat from 0 h to 50 h at the current density of 2 mA cm^{-2} (Figure 3k,l and Figure S6a,b). Almost no significant irregular flakes or filaments are observed on the surface of the Zn/PDZ-H anode even after the cycling time of 1,350 h (Figure 3m and Figure S6c). These results are corresponded nicely to the LCSM images of Figure 3e-g, which demonstrates that the PDZ-H electrolyte can effectively suppress the growth of Zn dendrites. In addition, the SEM images of the Zn/PZ-H anode at different cycling times in Figure S7 in the Supporting Information exhibit that the Zn dendrites are dramatically inhibited in comparison to that of the Zn/Z-AE anode.

2.3 Synthesis and Structural Characterization of $Zn_3V_2O_8$ Nanosheets Cathode and Electrochemical Performance of $Zn_3V_2O_8$//Zn/PDZ-H full cell

To further demonstrate the highly reversible Zn plating and stripping of Zn/PDZ-H in actual full cells, $Zn_3V_2O_8$ nanosheets are used as the cathode to assemble the ZIBs. As shown in Figure S8a, Supporting Information, the formation of $Zn_3V_2O_8$ is verified by X-ray diffraction (XRD). All characteristic peaks in the XRD pattern can be corresponded to the orthorhombic $Zn_3V_2O_8$ phase (PDF#34-0378). Lattice parameters (a = 6.1193 Å, b = 11.5314 Å, and c = 8.2975 Å) can be obtained from the corresponding Rietveld refined profile, which is almost consistent with the crystal structure of $Zn_3V_2O_8$. The corresponding orthorhombic crystal structure is depicted in Figure S8b (Supporting Information). As shown in Figure S8c,d, Supporting Information, the morphology and microstructure of $Zn_3V_2O_8$ are investigated by SEM and transmission electron microscopy (TEM). The SEM and TEM images of the $Zn_3V_2O_8$ show the uniform nanosheets with a length of 300 ~ 500 nm. The distribution of Zn, V and O elements in the $Zn_3V_2O_8$ nanosheets is mapped and demonstrated to be quite homogeneous by energy dispersive spectroscopy (EDS) (Figure S9, Supporting Information). In addition, a lattice spacing of 0.31 nm is observed in the high-resolution

TEM (HRTEM) image, which is consistent with the (131) plane of $Zn_3V_2O_8$ (Figure S8d, Supporting Information).

To investigate the Zn ion storage performance of $Zn_3V_2O_8$, we construct the aqueous ZIBs based on $Zn_3V_2O_8$ cathodes, Zn foil anodes and PDZ-H electrolyte (**Figure 4**a). From the CV curves of $Zn_3V_2O_8$//Zn/PDZ-H full cell at various scan rates (Figure 4b), the two obvious cathodic peaks locate at 0.78 and 1.12 V, and the two anodic peaks at 0.47 and 0.83 V that are corresponded to their reversible process, representing the Zn ion intercalation and de-intercalation process within the cathode. The galvanostatic charge/discharge (GCD) profiles at different current densities are exhibited in Figure 4c. The almost symmetric charge and discharge curves demonstrate an excellent reversibility and two well-defined discharge plateau. A large specific capacity of 265.2 mAh g^{-1} is achieved at the current density of 0.2 A g^{-1}, and a specific capacity of 185.1 mAh g^{-1} can be obtained even at a high current density of 10 A g^{-1}. Moreover, the $Zn_3V_2O_8$//Zn/PDZ-H full cell demonstrates a superior rate capability with reversible capacities of 265.2, 251.1, 237.8, 219.4, 200.8, and 185.1 mAh g^{-1} at the current densities of 0.2, 0.5, 1, 2, 5, and 10 A g^{-1}, respectively (Figure 4d). Furthermore, the specific capacity of the $Zn_3V_2O_8$//Zn/PDZ-H cell can be recovered to 255.6 mAh g^{-1} when the current density returns to 0.2 A g^{-1} (Figure 4d). The long-term cycling performance of $Zn_3V_2O_8$//Zn/PDZ-H full cell at 1 A g^{-1} is exhibited in Figure 4e, and a high discharge capacity retention of 95.27 % is achieved after 3,000 cycles.

To verify the superiority of the Zn/PDZ-H anode, the electrochemical performance of $Zn_3V_2O_8$//Zn/Z-AE cell based on $Zn_3V_2O_8$ cathode and the Zn/Z-AE anode was also measured for comparison (Figure S10, Supporting Information). The CV curve of the $Zn_3V_2O_8$//Zn/PDZ-H full cell is compared with that of the $Zn_3V_2O_8$//Zn/Z-AE cell obtained at a scan rate of 5 mV s^{-1}. The $Zn_3V_2O_8$//Zn/PDZ-H displays larger curve area (higher capacity) and smaller polarization of 21 mV (Figure S11a, Supporting Information). As shown in Figure S11b in the Supporting Information, the typical charge/discharge curve of the $Zn_3V_2O_8$//Zn/PDZ-H full cell at 0.5 A g^{-1} exhibits a narrower voltage gap than that of the $Zn_3V_2O_8$//Zn/Z-AE cell. The differences of the above performance can be attributed to different R_{ct} and ion migration behavior, which can be further verified by their electrochemical impedance spectroscopy (EIS) results. Compared with the $Zn_3V_2O_8$//Zn/Z-AE cell, the $Zn_3V_2O_8$//Zn/PDZ-H full cell exhibits an angle higher than 45° in the low-frequency region, which suggests the low diffusion resistance of the PDZ-H electrolyte (Figure S11c and Figure S12, Supporting Information).[30] Figure 4f reveals the CV curve of the $Zn_3V_2O_8$//Zn/PDZ-H full cell at a scan rate of 10 mV s^{-1}. The capacitive contribution accounts for 91.2 % of the whole capacity, indicating the partial capacitance contribution of the $Zn_3V_2O_8$ electrode, enabling the realization of the higher rate capability. In addition, the capacitive contributions at different scan rates are shown in Figure 4g. The capacitive-controlled kinetics become more evident as the scan rate increases, which demonstrates the fast kinetics and ion diffusion of $Zn_3V_2O_8$//Zn/PDZ-H full cell.[31] Ragone plot in Figure 4h exhibits that the $Zn_3V_2O_8$//Zn/PDZ-H full cell delivers a high energy density of 412.3 Wh Kg^{-1} at a power density of 206.1 W kg^{-1}, which has significantly exceeded the previously reported aqueous ZIBs (Table S1, Supporting Information).[32-47]

2.4 Electrochemical Properties of $Zn_3V_2O_8$//Zn/PDZ-H Full Cell in a Wide Temperature Range

Figure 5a shows a schematic diagram of the PDZ-H electrolyte with environmental adaptability. In this hydrogel, PAAm with a unique three-dimensional cross-linking network structure can withstand excessive high or low temperature.[48] In addition, DMSO can form strong hydrogen bonds with water molecules, which not only inhibits the passivation of Zn surface and enhances the Zn plating/stripping, but also forms the H_2O/DMSO binary solution and further achieves a low freezing point and high thermal stability of the PDZ-H electrolyte.[49] Figure 5b exhibits the CV curves of the $Zn_3V_2O_8$//Zn/PDZ-H full-cell at a scan rate of 2 mV s^{-1} at temperatures ranging from - 40 to 60 °C. Obviously, all of the redox peaks remain well profiled when the temperature ranges from - 40 to 60 °C. Besides, the two cathodic peaks move to lower potential values and the two anodic peaks shift to higher potential values when the temperature declines. These results are derived from the reduced ion transport kinetics of the $Zn_3V_2O_8$//Zn/PDZ-H full cell at low temperature.[50] More importantly, the GCD curves measured at temperatures of - 40 to 60 °C demonstrate that the characteristic of the two-step charge storage mechanism of charge/discharge process does not change with the variation of temperature (Figure 5c). The discharge capacity of 78.9 % can be retained at 0.5 A g^{-1} when the temperature decreases from room temperature (RT) to an extremely low value of - 40 °C, indicating the outstanding environmental adaptability of the as-fabricated $Zn_3V_2O_8$//Zn/PDZ-H cell. Figure S13 in the Supporting Information displays the Nyquist plots of the $Zn_3V_2O_8$//Zn/PDZ-H full cell at different temperatures, and the almost vertical lines at low frequency region are well retained thought the temperature range of - 40 °C to 60 °C, revealing a stable charge transport in $Zn_3V_2O_8$//Zn/PDZ-H cell. In addition, the value of R_{ct} of the as-fabricated $Zn_3V_2O_8$//Zn/PDZ-H full cell can reach 268.4 Ω at - 40 °C, which is very close to the value of R_{ct} at RT, demonstrating the anti-freezing ability of the obtained ZIBs. Moreover, the $Zn_3V_2O_8$//Zn/PDZ-H full cell possesses the extraordinary temperature-resistance properties under temperature fluctuation two tests and cycle performance test at low environmental temperature (Figure S14, Supporting Information). This achieves a stable operation over 2,300 cycles with a current density of 0.2 A g^{-1} at - 40 °C, and CE of the $Zn_3V_2O_8$//Zn/PDZ-H full cell is nearly 100 %. Furthermore, the rate capability of the $Zn_3V_2O_8$//Zn/PDZ-H full cell at different temperatures is presented in Figure S15 in the Supporting Information. The discharge capacity of the $Zn_3V_2O_8$//Zn/PDZ-H full cell still can be recovered to 96 % of its initial capacity even when the current density increases from 0.2 to 10 A g^{-1} at different temperatures of -40,- 20, 0, 20 and 60 °C and then returns to 0.2 A g^{-1}. These results show that the PDZ-H electrolyte plays a significant role in inhibiting Zn dendrites growth during the long-term cycling measurement.[51] Surprisingly, the $Zn_3V_2O_8$//Zn/PDZ-H full cell achieves an unprecedented cyclic performance, and it can be operated over 300 days with the current density of 2 A g^{-1} at - 40°C (Figure 5d).

To demonstrate the potential application of the ZIBs based on the PDZ-H electrolyte at sub-zero temperatures, a coin cell fabricated with $Zn_3V_2O_8$//Zn/PDZ-H is placed in a transparent sink filled with ice, and it can successfully power an electronic watch at different temperatures for one hour (Figure 5e-h). A series connected unit with two coin cells yields an output voltage of ~ 3.4 V and discharge time was doubled when two coin cells were connected in parallel, indicating the scalability of the device in practical application (Figure S16a,b, Supporting Information). In addition, the tandem unit of cells placed in the ice bath can successfully light optical-fiber model lamps and power a light emitting diode (LED) with a Logo "HIT" (Figure 5i,j and Movie S1 Supporting Information). To further investigate the operation of cells at extremely low temperature, the tandem unit of cells is placed in the ice bath and filled into liquid nitrogen. Electric windmills can be powered at a temperature as low as - 40°C (Figure 5k and Movie S2 Supporting Information).

2.5 Energy Storage Mechanism of the $Zn_3V_2O_8$//Zn/PDZ-H full cell

Significant insight into the phase evolution and stability of the $Zn_3V_2O_8$ cathode as well as the Zn ion storage mechanism of the $Zn_3V_2O_8$//Zn/PDZ-H full cell are investigated by ex-situ XRD and X-ray photoelectron spectroscopy (XPS) measurements. The ex-situ XRD results of the $Zn_3V_2O_8$ cathode exhibit the structural evolution during the galvanostatic discharge/charge processes, and the spheres with different colours represent different potential windows (**Figure 6**a). Obviously, the relative intensities of the characteristic peaks of $Zn_3V_2O_8$ gradually decrease and shift to smaller angles during the first charge process. The two characteristic peaks located at 12.5° and 24.7° correspond to (001) and (002) crystal planes of $Zn_3(OH)_2V_2O_7\cdot 2H_2O$, respectively. Partial vanadium oxide is formed after the cell is fully charged to 1.8 V due to de-intercalation of Zn^{2+} from cathode. And the small characteristic peaks of $Zn_3(OH)_2V_2O_7\cdot 2H_2O$ and V_2O_5 still exist after the second charging/discharging process, which is attributed to the slightly irreversible phase transition within the cathode material.[33] However, the main peaks of $Zn_3V_2O_8$ move back to the initial state, suggesting a reversible structure change of $Zn_3V_2O_8$ cathode during the repeated charge/discharge process.

The reversible intercalation reaction of $Zn_3V_2O_8$ cathode is also verified by the ex-situ XPS measurement. Figure 6b presents that only one peak of Zn 2p 3/2 (1022.2 eV) in the Zn 2p region during in the initial and fully charged stages (Charge to 1.8 V), arising from Zn^{2+} sites in the $Zn_3V_2O_8$ electrode. After full discharge state (Discharge to 0.2 V), a novel peak of Zn 2p 3/2 at 1021.2 eV appears, which is due to the successful insertion of Zn^{2+} into the open structure of $Zn_3V_2O_8$. Correspondingly, the intensity of the V^{5+} peak is markedly consolidated in the initial and full charge state. Subsequently, partial V^{5+} is reduced to $V^{\delta+}$ ($\delta < 5$) due to intercalation of Zn^{2+} when the discharge process sustains to full discharge state (Figure 6c). Moreover, the peak of $V^{\delta+}$ disappears upon charging to 1.8 V, which also reveal that the $Zn_3V_2O_8$ cathode embraces the outstanding structural reversibility and stability.

Possible migration pathways for Zn^{2+} in $Zn_3V_2O_8$ cathode are estimated based on density functional theory (DFT) calculations.[52-56] As shown in Figure 6d,e, three different and stable Zn sites can be found, which are denoted as Zn1, Zn2 and Zn3, respectively (Figure 6d). Among them, Zn2 possesses the lowest energy and can be regarded as a reference point (0 eV). When Zn ions migrate from Zn2 to Zn1 (corresponding to [001] direction) and Zn3 (corresponding to [010] direction), the potential barriers are 2.351 and 3.566 eV at least, which are significantly greater than the potential barrier of Zn ions migrating from a Zn2 site to another adjacent Zn2 site (corresponding to [100] direction). Therefore, the most likely diffusion path of Zn ions is along [100] direction. The nudge elastic band (NEB) calculation for Zn ion diffusion path along [100] direction in Figure 6f indicates that the actual energy barrier is ~ 1.635 eV, which means that a minimum diffusion barrier along the [100] direction is obtained due to the existing of large interstitial sites at the Zn2 position.[57] It is conducive to fast Zn^{2+} migration as well as high rate performance of the $Zn_3V_2O_8$ cathode. In addition, the density of states (DOS) and partial density of states (PDOS) in Figure 6g show that the $Zn_3V_2O_8$ cathode embraces a band gap of 2.26 eV, thus it can be utilized as ideal cathode materials for ZIBs.

3. Conclusion

In summary, We have successfully developed a novel cross-linking PDZ-H electrolyte with excellent mechanical performance to inhibit Zn dendrites growth and improve the reversibility of Zn metal anodes via the combination of the PAAm zincophilic group and DMSO additive. Benefitting from the excellent synergistic effect of PAAm and DMSO, the high reversibility of the Zn anode in the PDZ-H electrolyte is achieved, which can be maintained over 1,300 h. In addition, the $Z_3V_2O_8$//Zn/PDZ-H full cell delivers a high energy density of 412.3 Wh kg^{-1} and a superior cycling stability with the capacity retention of 95.27 % at 1 A g^{-1} after 3,000 cycles. Moreover, this full-cell system can be contiguously operated at a wide operating temperature from - 40 to 60 °C, and achieves stable operation over 75,000 cycles with a current density of 2 A g^{-1} at - 40 °C. This work provides a facile fabrication strategy to construct multi-component hydrogel electrolyte for high-performance Zn ion energe storage devices with excellent environmental adaptability.

Supporting Information

Supporting Information is available from the Wiley Online Library or from the author.

Acknowledgements

This work was supported by the Natural Science Foundation of Shandong Province China, (ZR202102220704) and the Research Grants Council of Hong Kong (RGC Postdoctoral Fellowship Scheme, Grant No.: PDFS2122-5S03).

Received: ((will be filled in by the editorial staff))
Revised: ((will be filled in by the editorial staff))
Published online: ((will be filled in by the editorial staff))

References

[1] D. Chen, Z. Lou, K. Jiang, G. Shen, Adv. Funct. Mater. 2018, 28, 1805596.

[2] K. Adair, M. Iqbal, C. Wang, Y. Zhao, M. Banis, R. Li, L. Zhang, R. Yang, S. Lu, X. Sun, *Nano Energy* **2018**, *54*, 375-382.

[3] T. Liu, Y. Yu, X.-Y. Yang, J. Wang, X.-B. Zhang, *Small Struct.* **2020**, *1*, 2000015.

[4] X. Feng, M. Ouyang, X. Liu, L. Lu, Y. Xia, X. He, *Energy Storage Mater.* **2018**, *10*, 246-267.

[5] Q. Zhang, C. Li, Q. Li, Z. Pan, J. Sun, Z. Zhou, B. He, P. Man, L. Xie, L. Kang, X. Wang, J. Yang, T. Zhang, P.P. Shum, Q. Li, Y. Yao, L. Wei, *Nano Lett.* **2019**, *19*, 4035-4042.

[6] J. Pu, K. Zhang, Z. Wang, C. Li, K. Zhu, Y. Yao, G. Hong, *Adv. Funct. Mater.* **2021**, *31*, 2106315.

[7] Z. Shen, Z. Tang, C. Li, L. Luo, J. Pu, Z. Wen, Y. Liu, Y. Ji, J. Xie, L. Wang, Y. Yao, G. Hong, *Adv. Energy Mater.* **2021**, *11*, 2102055.

[8] Y. Zhao, Y. Zhu, X. Zhang, InfoMat. 2020, 2, 237-260.

[9] H. Wu, F. Ming, Y. Lei, W. Zhang, H. N. Alshareef, *Small Struct.* **2020**, *1*, 2000040.

[10] B. He, Q. Zhang, P. Man, Z. Zhou, C. Li, Q. Li, L. Xie, X. Wang, H. Pang, Y. Yao, *Nano Energy* **2019**, *64*, 103935.

[11] M. Chen, J. Chen, W. Zhou, X. Han, Y. Yao, C.-P. Wong, *Adv. Mater.* **2021**, *33*, 2007559.

[12] Y. Wu, M. Wang, Y. Tao, K. Zhang, M. Cai, Y. Ding, X. Liu, T. Hayat, A. Alsaedi, S. Dai, *Adv. Funct. Mater.* **2019**, *30*, 1907120.

[13] P. Liang, J. Yi, X. Liu, K. Wu, Z. Wang, J. Cui, Y. Liu, Y. Wang, Y. Xia, J. Zhang, *Adv. Funct. Mater.* **2020**. *30*, 201908528.

[14] C. Liu, X. Xie, B. Lu, J. Zhou, S. Liang, *ACS Energy Lett.* **2021**, *6*, 1015-1033.

[15] C. Wang, Z. Pei, Q. Meng, C. Zhang, X. Sui, Z. Yuan, S. Wang, Y. Chen, *Angew. Chem. Int. Ed.* **2021**, *60*, 990-997.

[16] P. Yang, C. Feng, Y. Liu, T. Cheng, X. Yang, H. Liu, K. Liu, H.J. Fan, *Adv. Energy Mater.* **2020**, *10*, 2002898.

[17] X. Wu, Y. Xu, C. Zhang, D. Leonard, A. Markir, J. Lu, X. Ji, *J. Am. Chem. Soc.* **2019**, *141*, 6338-6344.

[18] S. Banik, R. Akolkar, *Electrochim. Acta* **2015**, *179*, 475-481.

[19] C. Li, X. Xie, S. Liang, J. Zhou, *Energy Environ. Mater.* **2020**, *3*, 146-159.

[20] M. Zhu, X. Wang, H. Tang, J. Wang, Q. Hao, L. Liu, Y. Li, K. Zhang, O. Schmidt, *Adv. Funct. Mater.* **2020**, *30*, 1907218.

[21] J. Cong, X. Shen, Z. Wen, X. Wang, L. Peng, J. Zeng, J. Zhao, *Energy Storage Mater.* **2021**, *35*, 586-594.

[22] Q. Nian, J. Wang, S. Liu, T. Sun, S. Zheng, Y. Zhang, Z. Tao, J. Chen, *Angew. Chem. Int. Ed.* **2019**, *58*,16994-16999.

[23] L. Cao, D. Li, E. Hu, J. Xu, T. Deng, L. Ma, Y. Wang, X.Q. Yang, C. Wang, *J. Am. Chem. Soc.* **2020**, *142*, 21404-21409.

[24] M. Gupta, R. Bansil, *J. Polym. Sci., Polym. Phys. Ed.* **1981**, *19*, 353.

[25] N. Zhang, F. Cheng, Y. Liu, Q. Zhao, K. Lei, C. Chen, X. Liu, J. Chen, *J. Am. Chem. Soc.* **2016**, *138*, 12894-12901.

[26] Z. Zhao, J. Zhao, Z. Hu, J. Li, J. Li, Y. Zhang, C. Wang, G. Cui, *Energy Environ. Sci.* **2019**, *12*, 1938-1949.

[27] S. Guo, S. Liang, B. Zhang, G. Fang, D. Ma, J. Zhou, *ACS Nano* **2019**, *13*, 13456-13464.

[28] Y. Zeng, X. Zhang, R. Qin, X. Liu, P. Fang, D. Zheng, Y. Tong, X. Lu, *Adv. Mater.* **2019***, 31*, 1903675.

[29] X. Xie, S. Liang, J. Gao, S. Guo, J. Guo, C. Wang, G. Xu, X. Wu, G. Chen, J. Zhou, *Energy Environ. Sci.* **2020**, *13*, 503-510.

[30] J. Zhao, Y. Zhang, Y. Huang, J. Xie, X. Zhao, C. Li, J. Qu, Q. Zhang, J. Sun, B. He, Q. Li, C. Lu, X. Xu, W. Lu, L. Li, Y. Yao, *Adv. Sci.* **2018**, *5*, 1801114.

[31] Y. Li, P. Lu, P. Shang, L. Wu, X. Wang, Y. Dong, R. He, Z.-S. Wu, *J. Energy Chem.* **2021**, *56*, 404-411.

[32] W. Deng, Z. Li, Y. Ye, Z. Zhou, Y. Li, M. Zhang, X. Yuan, J. Hu, W. Zhao, Z. Huang, C. Li, H. Chen, J. Zheng, R. Li, *Adv. Energy Mater.* **2021**, *11*, 2003639.

[33] D. Chao, C. Zhu, M. Song, P. Liang, X. Zhang, N.H. Tiep, H. Zhao, J. Wang, R. Wang, H. Zhang, H. Fan, *Adv. Mater.* **2018**, *30*, 1803181.

[34] Q. Cao, H. Gao, Y. Gao, J. Yang, C. Li, J. Pu, J. Du, J. Yang, D. Cai, Z. Pan, C. Guan, W. Huang, *Adv. Funct. Mater.* **2021**, *31*, 2103922.

[35] L. Ma, S. Chen, C. Long, X. Li, Y. Zhao, Z. Liu, Z. Huang, B. Dong, J. Zapien, C. Zhi, *Adv. Energy Mater.* **2019**, *9*, 1902446.

[36] H. Luo, B. Wang, F. Wu, J. Jian, K. Yang, F. Jin, B. Cong, Y. Ning, Y. Zhou, D. Wang, H. Liu, S. Dou, *Nano Energy* **2021**, *81*, 105601.

[37] T. He , S. Weng, Y. Ye, J. Cheng, X. Wang, X. Wang, B. Wang, *Energy Storage Mater.* **2021**, *38*, 389-396.

[38] J. Wu, Q. Kuang, K. Zhang, J. Feng, C. Huang, J. Li, Q. Fan, Y. Dong, Y. Zhao, *Energy Storage Mater.* **2021**, *41*, 297-309.

[39] F. Liu, Z. Chen, G. Fang, Z. Wang, Y. Cai, B. Tang, J. Zhou, S. Liang, *Nano-Micro Lett.* **2019**, *11*, 25.

[40] K. Lu, B. Song, Y. Zhang, H. Ma, J. Zhang, *J. Mater. Chem A* **2017**, *5*, 23628-23633.

[41] K. Zhu, T. Wu, W. Bergh, M. Stefik, K. Huang, *ACS Nano* **2021**, *15*, 10678-10688.

[42] Y. Dong, S. Di, F. Zhang, X. Bian, Y. Wang, J. Xu, L. Wang, F. Cheng, N. Zhang, *J. Mater. Chem. A* **2020**, *8*, 3252-3261.

[43] C. Liu, W. Xu, C. Mei, M. Li, W. Chen, S. Hong, W.Y. Kim, S.y. Lee, Q. Wu, *Adv. Energy Mater.* **2021**, *11*, 2003902.

[44] Y. Cai, F. Liu, Z. Luo, G. Fang, J. Zhou, A. Pan, S. Liang, *Energy Storage Mater.* **2018**, *13*, 168-174.

[45] M. Chae, J. Heo, H. Kwak, H. Lee, S.-T. Hong, *J. Power Sources* **2017**, *337*, 204-211.

[46] V. Renman, D. Ojwang, M. Valvo, C. Gómez, T. Gustafsson, G. Svensson, *J. Power Sources* **2017**, *369*, 146-153.

[47] X. Wang, B. Xi, X. Ma, Z. Feng, Y. Jia, J. Feng, Y. Qian, S. Xiong, *Nano Lett.* **2020**, *20*, 2899-2906.

[48] Y. Wei, L. Xiang, P. Zhu, Y. Qian, B. Zhao, G. Chen, *Chem. Mater.* **2021**, *33*, 8623-8634.

[49] Q. Nian, X. Zhang, Y. Feng, S. Liu, T. Sun, S. Zheng, X. Ren, Z. Tao, D. Zhang, J. Chen, *ACS Energy Lett.* **2021**, *6*, 2174-2180.

[50] W. Deng, Z. Zhou, Y. Li, M. Zhang, X. Yuan, J. Hu, Z. Li, C. Li, R. Li, *ACS Nano* **2020**, *14*, 15776-15785.

[51] Y. Sun, H. Ma, X. Zhang, B. Liu, L. Liu, X. Zhang, J. Feng, Q. Zhang, Y. Ding, B. Yang, L. Qu, X. Yan, *Adv. Funct. Mater.* **2021**, *31*, 2101277.

[52] G. Kresse, J. Furthmüller, *Comput. Mater. Sci.* **1996**, *6*, 15-50.

[53] G. Kresse, J. Hafner, *Phys. Rev. B* **1994**, *49*, 14251-14269.

[54] P. Blöchl, O.Jepsen, O. Andersen, *Phys. Rev. B* **1994**, *49*, 16223-16233.

[55] G. Kresse, D. Joubert, *Phys. Rev. B* **1999**, *59*, 1758-1775.

[56] J. Perdew, K. Burke, M. Ernzerhof, *Phys. Rev. Lett.* **1996**, *77*, 3865-3868.

[57] G. Henkelman, B. Uberuaga, H. Jonsson. J. Chem. Phys. **2000**, *113*, 9901-9904.

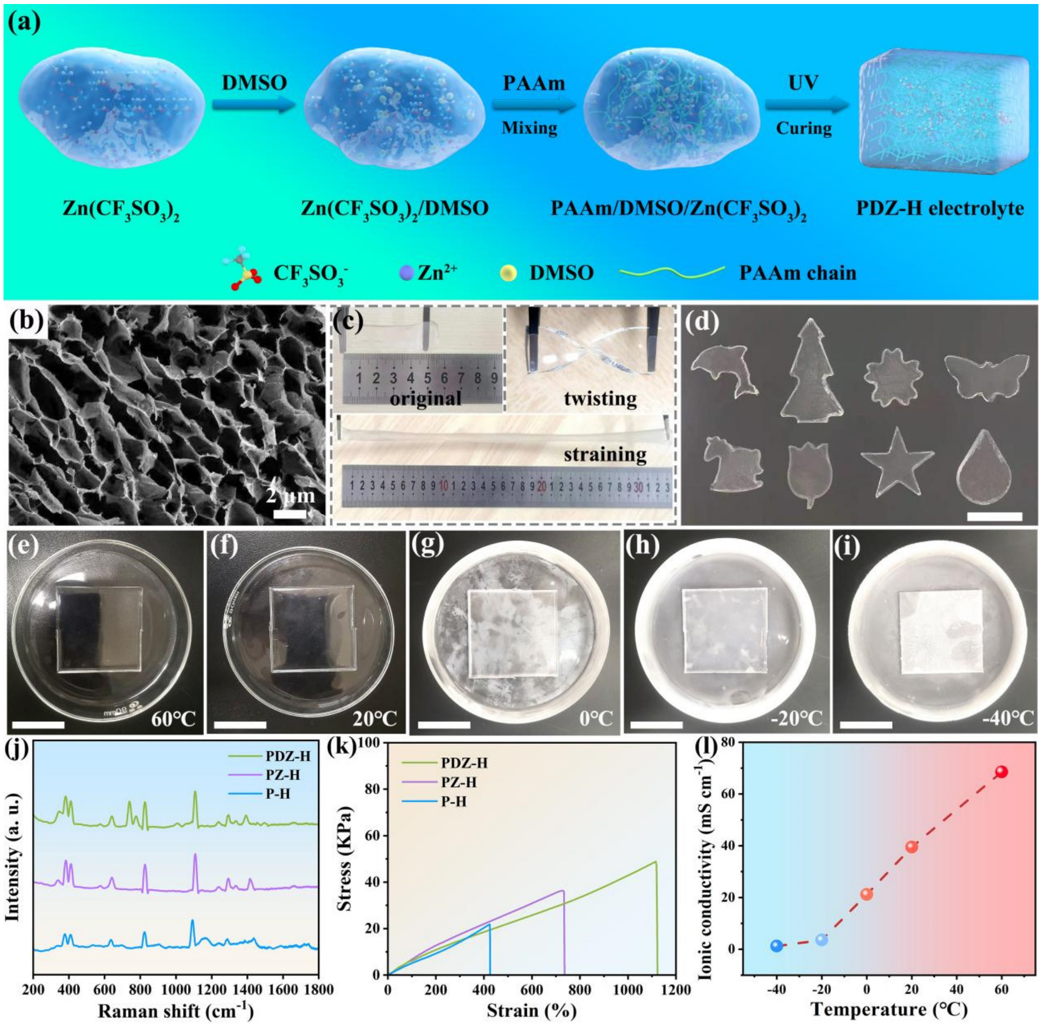

Figure 1. (a) Schematic diagram of synthesis process of the PDZ-H electrolyte. (b) SEM image of the PDZ-H electrolyte. Optical photo of original, twisted and strained PDZ-H electrolytes (c) and PDZ-H electrolyte in various patterns (d). (e)-(i) Digital photos of PDZ-H electrolyte at different temperatures from 60 to - 40 °C. Scale bar: 2 cm. (j) The Raman spectra of the PDZ-H, PZ-H and P-H electrolyte. (k) Stress-strain curves of PDZ-H, PZ-H and P-H electrolytes. (l) The ionic conductivity of the PDZ-H electrolyte at different temperature.

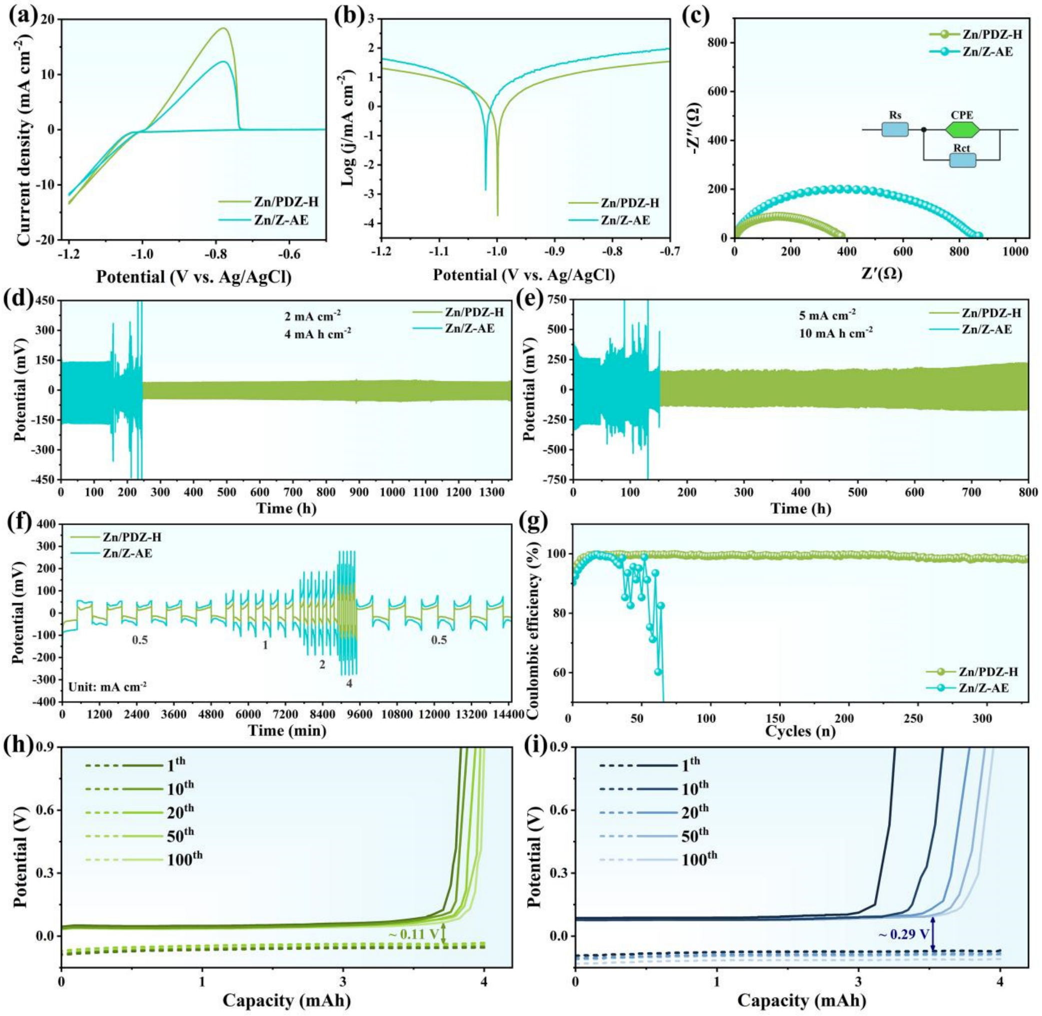

Figure 2. (a) CV curves, (b) linear polarization curves and (c) Nyquist plots of Zn/PDZ-H and Zn/Z-AE anodes. Voltage profiles of symmetric cells based on Zn/PDZ-H and Zn/Z-AE anodes at 2 mA cm^{-2} (d) and 5 mA cm^{-2} (e). (f) Rate performance of the symmetric cells based on Zn/PDZ-H and Zn/Z-AE at current densities from 0.5 to 5 mA cm^{-2}. (g) Coulombic efficiency of the symmetric cells based on Zn/PDZ-H and Zn/Z-AE anodes at 2 mA cm^{-2}. Voltage profiles of the Zn/PDZ-H (h) and Zn/Z-AE anode (i) at 2 mA cm^{-2} with the capacity limited to 4 mAh cm^{-2}.

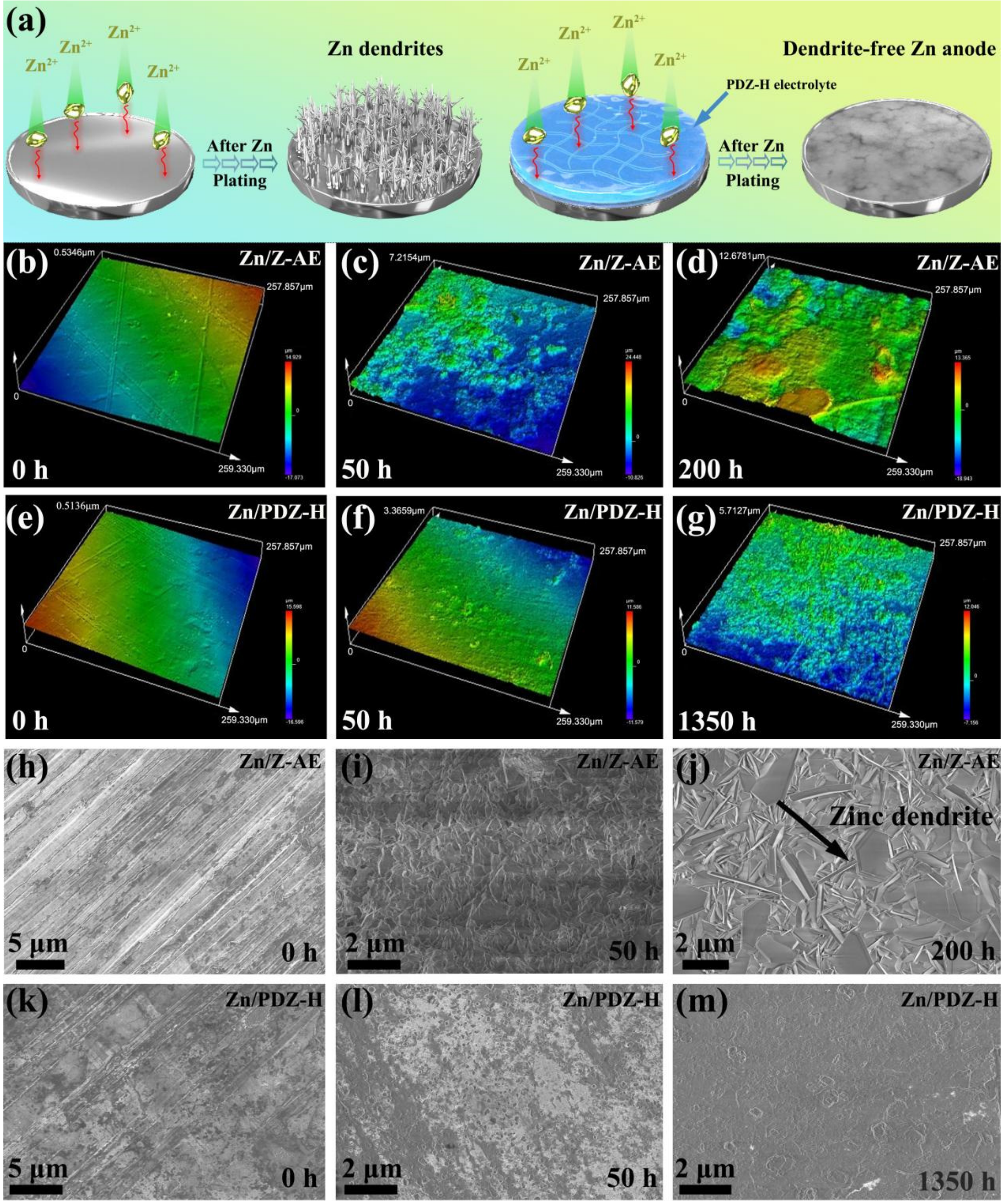

Figure 3. (a) Schematic illustration of Zn plating on Zn/Z-AE and Zn/PDZ-H. LCSM images of the Zn/Z-AE anode in the Zn/Z-AE//Zn/Z-AE symmetric cell after different cycling time of 0 h (b), 50 h (c) and 200 h (d), respectively, and the Zn/PDZ-H anode in the Zn/PDZ-H//Zn/PDZ-H symmetric cell after different cycling times of 0 h (e), 50 h (f) and 1350 h (g), respectively. High-magnification SEM images of Zn/Z-AE in the Zn/Z-AE//Zn/Z-AE symmetric cell after different cycling times of 0 h (h), 50 h (i) and 200 h (j), respectively, and the Zn/PDZ-H anode in the Zn/PDZ-H//Zn/PDZ-H

symmetric cell after different cycling times of 0 h (k), 50 h (l) and 1350 h (m), respectively.

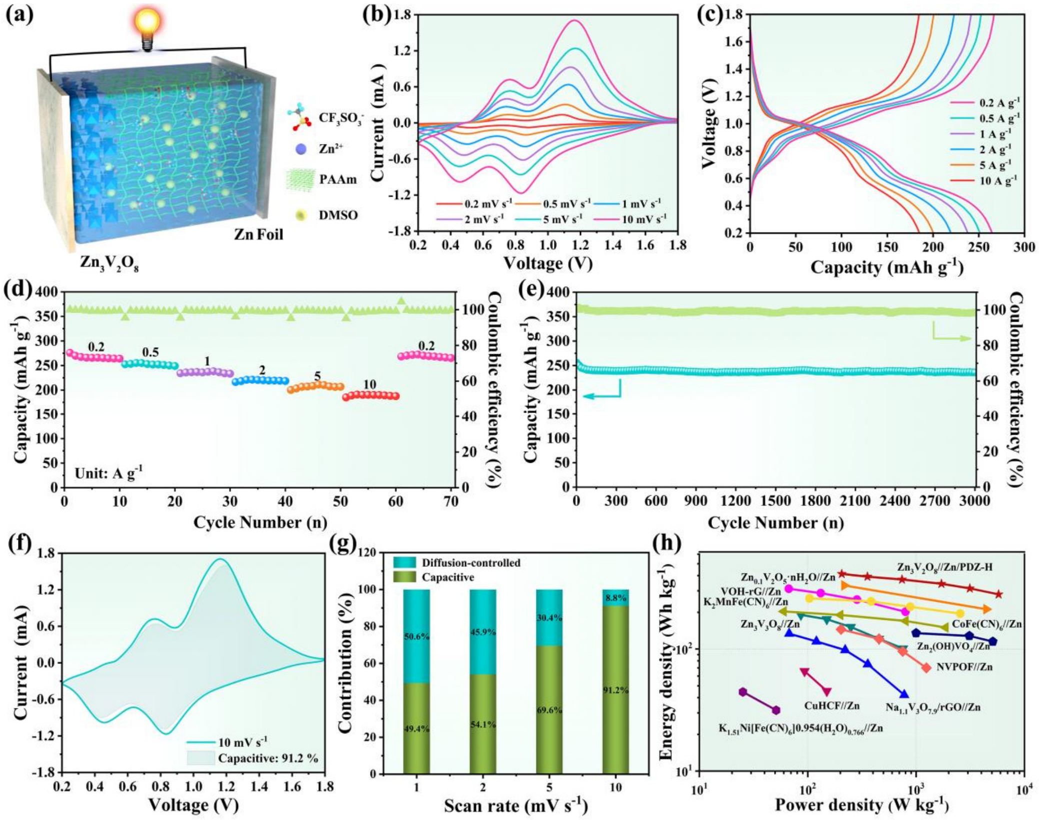

Figure 4. (a) Schematic of the Zn$_3$V$_2$O$_8$//Zn/PDZ-H full cell. (b) CV curves of the Zn$_3$V$_2$O$_8$//Zn/PDZ-H full cell at different scan rates. (c) GCD curves of Zn$_3$V$_2$O$_8$//Zn/PDZ-H full cell at different current densities. (d) Rate capability. (e) Long-term cycling performance of the Zn$_3$V$_2$O$_8$//Zn/PDZ-H full cell at the current density of 1 A g^{-1}. (f) Diffusion and capacitive contribution at 10 mV s^{-1}. (g) Normalized capacity contributions at different scan rates from 1 to 10 mV s^{-1}. (h) Ragone plots of Zn$_3$V$_2$O$_8$//Zn/PDZ-H full cell compared with previously reported Zn ion cell.[29, 30, 32, 33, 35, 38, 39, 41-43]

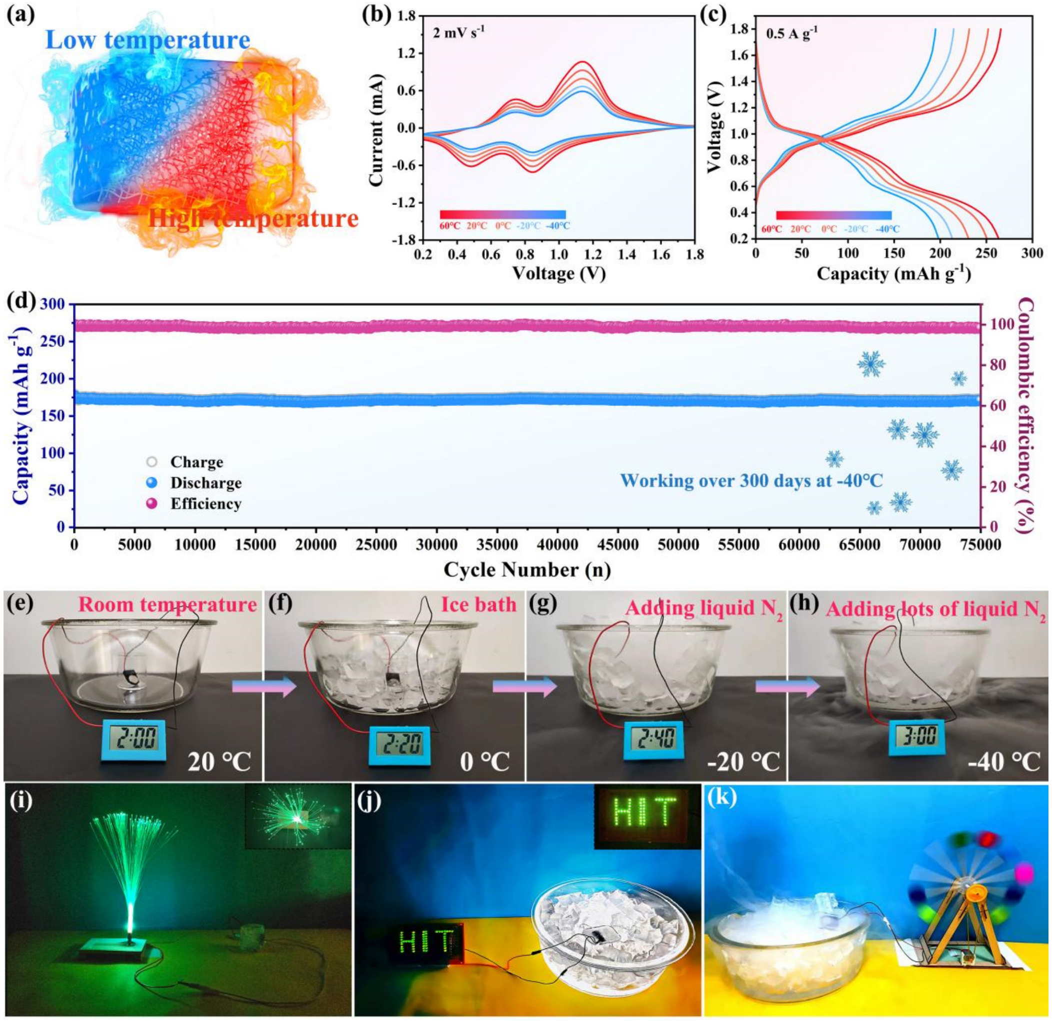

Figure 5. Electrochemical performance of $Zn_3V_2O_8$//Zn/PDZ-H full cells in a wide range of temperature and its practical application. (a) Schematic diagram of the PDZ-H electrolyte with environmental adaptability. (b) CV curves at various operating temperatures. (c) GCD curves at different temperature from 60 to - 40 °C. (d) Long-term cyclic stability of the $Zn_3V_2O_8$//Zn/PDZ-H full cell. (e)-(h) Photographs of a coin cell placed in a transparent sink filled with ice powering an electronic watch at different temperatures from 20 to -40 °C. (i) A photograph of a tandem unit of cell placed in an ice bath lighting up optical-fiber model lamps and (j) powering LEDs with a Logo "HIT". (k) A photograph of the tandem unit of cell placed in the an ice bath filled with liquid nitrogen driving electric windmills.

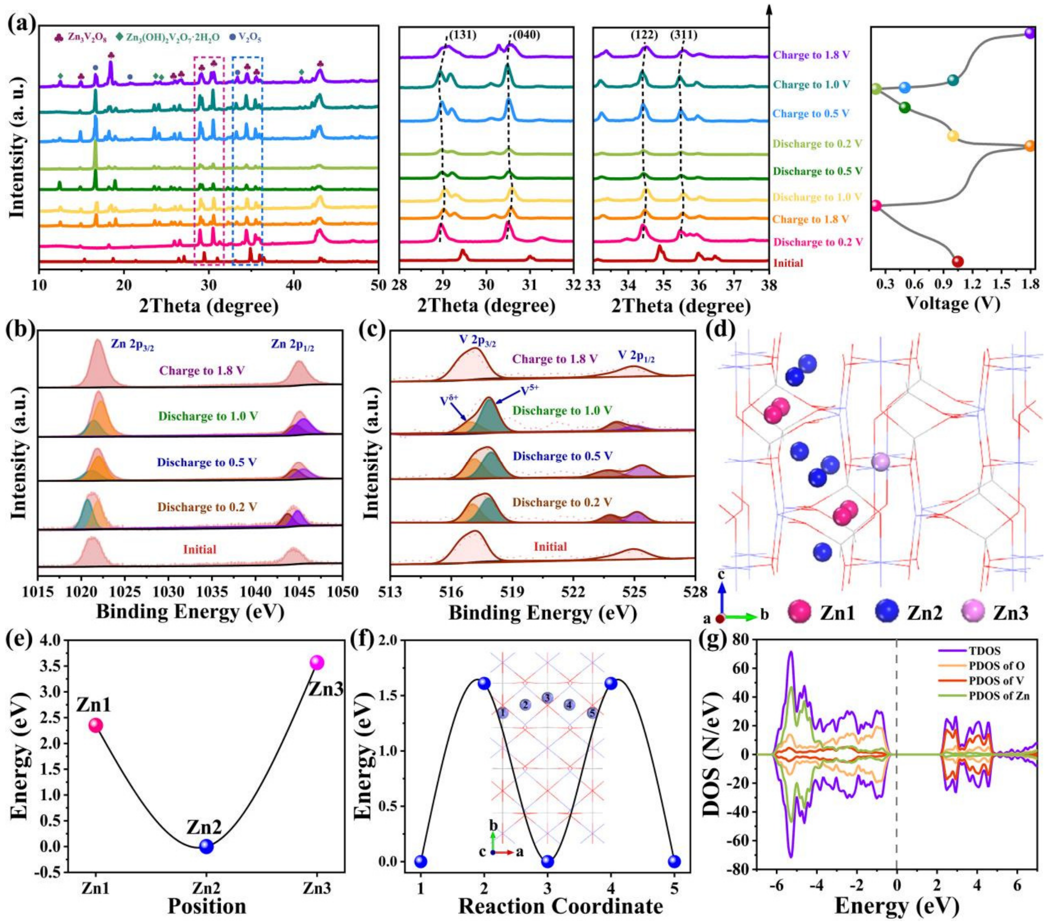

Figure 6. Investigation of reaction mechanisms of the $Zn_3V_2O_8$//Zn/PDZ-H full cell. (a) Ex-situ XRD patterns at various voltage stages collected during first discharge and the second galvanostatic discharge-charge profile at 0.2 A g^{-1}. Ex-situ high-resolution XPS spectra of (b) Zn 2p and (c) V 2p at different charge-discharge stages. (d) Molecular structure of $Zn_3V_2O_8$ as well as Zn^{2+} insertion (balls of different colors) with three different Zn occupation sites (denoted as Zn1, Zn2, and Zn3). (e) First-principle calculation of the energy barriers and the corresponding pathways for Zn-ion migration. (f) Energy barriers for Zn^{2+} diffusing along the [100] direction of $Zn_3V_2O_8$. (g) Density of state for $Zn_3V_2O_8$ cathode.